Broadband High-Frequency Power Modulation With Resistance Regulation Network

Zhechi Ye, *Graduate Student Member, IEEE*, Eric Stolt, *Graduate Student Member, IEEE*, Kawin Surakitbovorn, *Member, IEEE*, and Juan Rivas-Davila, *Senior Member, IEEE*

***Abstract*—Efficient radio frequency (RF) power amplifiers (PAs) are essential in various industrial applications, where fast RF pulses are often required to enhance system performance. In this article, we present a novel approach to fast RF power modulation using a resistance regulation network (RRN) with frequency adjustment. The proposed method is complementary to existing systems and can be adapted to a wide range of power and frequency levels. To illustrate the general design methodology of the RRN, we use an inductively coupled, double-tuned network as an example. We also discuss its loading effects and provide design guidelines for broadband switched-mode PAs. A 300 W class-Φ_2 amplifier with RRN is implemented and tested, achieving a peak efficiency of 94%. Operating between 13.2 and 14.4 MHz, the amplifier is capable of doubling its output power within 500 ns while maintaining zero-voltage-switching (ZVS).**

***Index Terms*—Frequency modulation, image impedance, power amplifier (PA), power modulation, resonant converter.**

I. Introduction

EFFICIENT radio frequency (RF) power amplifiers (PAs) are crucial components in a variety of industrial applications, such as plasma generation for semiconductor etching [1], induction heating [2], communication systems [3], and magnetic resonance imaging (MRI) [4]. Many of these applications also demand fast and precise RF power modulation to enhance performance and meet operational requirements [5], [6], [7], [8], [9], [10]. For instance, extremely low-frequency wave generation may require narrow RF power pulse widths as short as tens of microseconds to minimize conductivity losses [11]. Similarly, plasma-based semiconductor etching often demands a dynamic range greater than 20 dB to ensure precision and control during the etching process [12], [13], [14].

To achieve the desired large dynamic range and short power pulsewidths, various power modulation techniques are often combined to scale up power levels while balancing fast transients with efficient steady-state performance, as shown in Fig. 1.

Received 5 February 2025; revised 10 April 2025; accepted 29 April 2025. Date of publication 1 May 2025; date of current version 27 August 2025. Recommended for publication by Associate Editor J. Baek. *(Corresponding authors: Zhechi Ye; Kawin Surakitbovorn.)*

Zhechi Ye, Eric Stolt, and Juan Rivas-Davila are with the Department of Electrical Engineering, Stanford University, Stanford, CA 94305 USA (e-mail: yezc15@stanford.edu).

Kawin Surakitbovorn is with the School of International and Interdisciplinary Engineering Programs (SIIE), King Mongkut's Institute of Technology Ladkrabang, Bangkok 10520, Thailand (e-mail: Kawin.su@kmitl.ac.th).

Color versions of one or more figures in this article are available at https://doi.org/10.1109/TPEL.2025.3566326.

Digital Object Identifier 10.1109/TPEL.2025.3566326

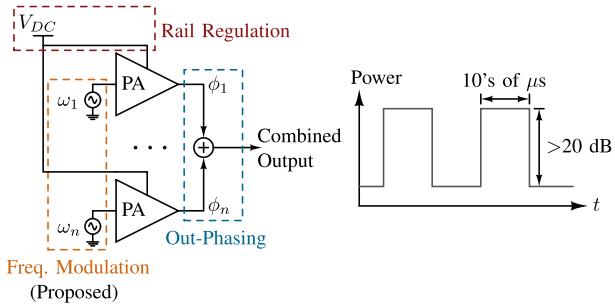

Fig. 1. Diagram of a pulsed RF power system with combined methods for power modulation: voltage rail regulation, out-phasing, and frequency modulation proposed in this article.

Existing methods for achieving fast RF power modulation primarily involve variations of rail voltage regulation [15], [16], [17] and out-phasing control [18], [19], [20], [21], each with its own set of advantages and limitations. The most common form of rail voltage regulation adjusts the dc supply voltage continuously to modulate the output power of amplifiers [4]. While this approach enables efficient transitions without compromising zero-voltage-switching (ZVS) of switched-mode amplifiers, the slew rate limitation due to the large dc bus capacitors slows down the system dynamics, limiting modulation speed. Zhang et al. [17] proposed a switched rail architecture that addresses the issue of slow transitions by incorporating multiple dc supplies. However, this solution sacrifices continuous tunability, and implementing reliable supply switches at RF remains a significant challenge. On the other hand, out-phasing amplifiers allow much faster power modulation by adjusting timing or even shutting down amplifiers or operating them in rectifier modes [17], [22]. However, multiphase systems require added complexity both in the physical component count and in the control. Moreover, even when utilizing an ideally "lossless" combiner network, the out-phasing converter's efficiency still tends to degrade when large phase shifts are applied [22].

In this manuscript, we propose a novel approach for highspeed RF power modulation using a resistance regulation network (RRN). By adjusting the frequency, the RRN modulates the equivalent load resistance seen by the amplifier, thereby controlling the delivered power. Table I highlights its key features in comparison to the aforementioned methods. Our approach enables ultrafast transition speeds, with demonstrated capability to double output power within approximately 500 ns at 13–14 MHz. Throughout these transitions, the amplifier maintains ZVS, ensuring high system efficiency. Furthermore, this

TABLE I
COMPARISON ON POWER MODULATION METHODS

	Speed	Efficiency	Complexity	Dynamic Range
Rail Volt. Regulation	Slow	High	Single-Phase	High
Switched Rail Volt.	Moderate	High	Multi-Rail	High
Out-phasing	Fast	Moderate	Multi-Phase	High
RRN Freq. Modulation	Fast	High	Single-Phase	Moderate

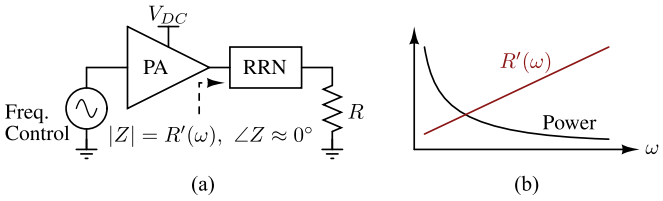

Fig. 2. (a) Conceptual diagram of the RRN. The RRN is connected to a resistive load R and powered by a broadband PA. It regulates the load impedance, presenting different driving point impedances (DPI, Z) at various frequencies. The DPI should exhibit a consistently resistive behavior across the frequency band. (b) Ideal illustration of power modulation with RRN. For a fixed PA output voltage, the DPI profile enables power modulation by adjusting the frequency.

method is compatible with both single- and multiphase systems and can be combined with existing power modulation techniques to provide improved performance and a wider dynamic range of power levels.

To maximize the system efficiency, the RRN power modulation technique is best utilized in conjunction with a switched-mode broadband PA. This article outlines the practical design guidelines for broadband switched-mode amplifiers and discusses the loading effects of the RRN. Section II introduces the concept and design of the RRN. Section III covers the design of broadband switched-mode PAs. Section IV presents the experimental results, where a 300 W class-Φ_2 prototype is implemented and tested, achieving a peak efficiency of 94%. Operating between 13.2 and 14.4 MHz, the amplifier is capable of doubling its output power within 500 ns while maintaining ZVS. Finally, Section V concludes this article.

II. RESISTANCE REGULATION NETWORK

In this section, we introduce the concept of an RRN and present a generalized methodology for designing such networks using image impedances. Fig. 2 illustrates a conceptual block diagram of the RRN, driven by a broadband PA and loaded by a constant resistance. We assume the PA is load-independent and generates a fixed output voltage. The RRN provides frequency-dependent impedance control, designed to exhibit different driving point impedance (DPI) values as the excitation frequency changes. Equivalently, the RRN transforms a fixed load into a controllable DPI so that the power delivered to the network can be modulated. Assuming a lossless network (e.g., an *LC* network), the output power equals the power delivered to the network and thus can be directly adjusted by tuning the frequency.

A trivial example of RRN is adding an inductor L between the amplifier and the load. The amplitude of its DPI is $\sqrt{R^2 + (\omega L)^2}$ with ω being the angular frequency. This frequency dependence theoretically enables power modulation, as the output current is inversely proportional to the DPI. However, this RRN is less practical due to the inductive nature of its DPI. First, most PAs are designed to drive resistive loads, making a variable inductive impedance highly undesirable. Such an impedance can lead to efficiency degradation and potential thermal issues in the amplifier. In addition, achieving significant power modulation may require a large frequency shift, which can strain the amplifier's bandwidth. For instance, at maximum power, we aim for the DPI to appear as resistive as possible to optimize semiconductor utilization within the amplifier. Assume that, as an engineering approximation, the load $R = 10\omega_0 L$ is chosen as ten times the reactance at some nominal frequency ω_0. This implies a tenfold increase in frequency would be required to roughly halve the delivered power, which is difficult to implement efficiently.

These challenges motivate the development of lossless RRNs with resistive DPI characteristics for improved efficiency and controllability. In the following sections, we present the general theory along with illustrative design examples of our proposed image impedance methodology, which offers an effective and straightforward approach for deriving such networks.

A. General Theory

The image impedances of a two-port network are defined such that when one port is terminated with its image impedance, the DPI at the other port matches the other image impedance [23], [25]. It is important to note that image impedances are specific to each port and are intrinsic properties of the unloaded network, determined solely by the network's structure. As shown in Fig. 3, we designate the port driven by the amplifier as port 1, with image impedance $Z_{i1}(\omega)$, and the port connected to the load as port 2, with image impedance $Z_{i2}(\omega)$. Both $Z_{i1}(\omega)$ and $Z_{i2}(\omega)$ are frequency dependent. When the network consists solely of lossless passive components, it is proven that both $Z_{i1}^2(\omega)$ and $Z_{i2}^2(\omega)$ are real numbers [23]. A key property of image impedance is that when a network is loaded with a load impedance that matches the magnitude and phase of the port's image impedance, the DPI at the other port will equal the image impedance of that port.

According to the definition, if $Z_{i2}(\omega) = R$ holds across the entire bandwidth of interest, the DPI of the network is simply $Z_{i1}(\omega)$. In other words, the frequency profile of $Z_{i1}(\omega)$ dictates the DPI value that loads the PA at any specific frequency, which in turn determines the output power. Since real power is always being delivered to the load, the designed image impedances are guaranteed to be purely resistive. Therefore, the DPI remains resistive as long as $Z_{i2}(\omega) = R$.

By shaping the frequency profile of $Z_{i1}(\omega)$, we can design how the output power is modulated with frequency variations. For example, a large derivative of $Z_{i1}(\omega)$ indicates more sensitive power modulation in response to frequency changes, while a convex $Z_{i1}(\omega)$ profile leads to a concave power-versus-frequency curve. Hence, our objective is to find

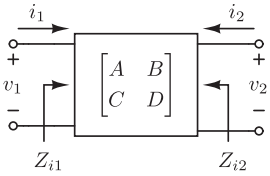

$$Z_{i1} = \sqrt{\frac{AB}{CD}}$$

$$Z_{i2} = \sqrt{\frac{BD}{AC}}$$

Fig. 3. Image impedances of a general two-port network. The network is specified by its $ABCD$ parameters with ports labeled accordingly in the figure. General expressions for the image impedances can be derived from these parameters, which are shown to the right of the network [23], [24].

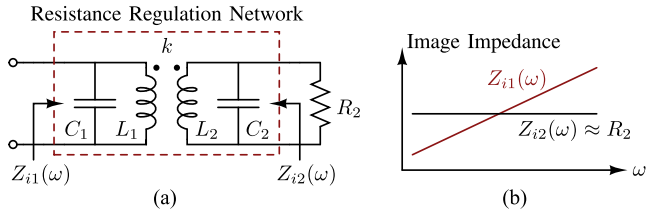

Fig. 4. (a) Schematic of the ICDT network as the RRN. The network consists of two inductors with a coupling coefficient k, and its image impedances are Z_{i1} and Z_{i2}. The network is loaded by a load resistance R_2. (b) Conceptual impedance curve showing the targeted image impedance profiles. Z_{i2} remains nearly constant with respect to R_2, while Z_{i1} depicts the intended DPI profile.

network) matches the load resistance R_2. This ensures that the resulting DPI equals Z_{i1}, which is also specified by our network design. Ideally, we would like $R_2 = Z_{i2}$ to hold strictly across the entire bandwidth of interest. However, this is not physically achievable with realistic *LC* networks. As a compromise, we can only have Z_{i2} approximately equal to R_2. As a result, the DPI will deviate from Z_{i1} in both amplitude and phase. However, by constraining the first or even higher order derivatives of $Z_{i2}(\omega)$ to zero, a good approximation can be achieved.

B. Inductively Coupled Double-Tuned (ICDT) RRN

To illustrate the proposed RRN design methodology, we present one specific example based on the ICDT network. Note that this is only one of many possible RRNs. The circuit diagram is shown in Fig. 4, with the coupling coefficient between the inductors denoted as k. The components are labeled with subscripts corresponding to their connected ports. Its image impedances can be derived as (1) and (2) shown at the bottom of this page.

Under nominal conditions, we assume the RRN regulates the load R_2 to a resistive DPI of R_1 at the angular frequency ω_0. In terms of image impedances, this is equivalent to satisfying

$$Z_{i1}(\omega_0) = R_1, \quad Z_{i2}(\omega_0) = R_2. \tag{3}$$

We then apply first-order approximations around this nominal point to constrain the desired image impedance profiles. As will

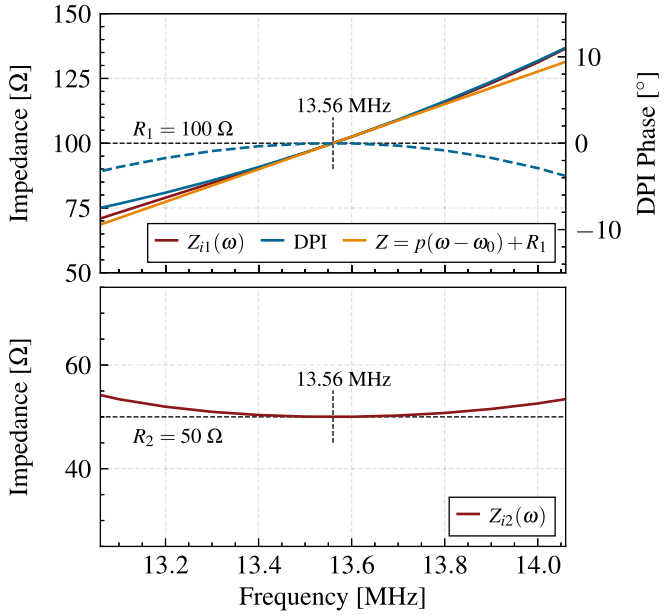

Fig. 5. Image impedance curves from the example RRN designed in Section II-B. The top curve compares the profile of the driver port image impedance $Z_{i1}(\omega)$, its linearized approximation around the nominal operating point and the loaded DPI. The amplitude of the DPI is represented by a solid line, while the phase is shown by a dashed line. The bottom curve shows the profile of the load port image impedance $Z_{i2}(\omega)$.

be shown, the resulting equations provide adequate accuracy across a wide variety of designs. To approximate $Z_{i2}(\omega) = R_2$ over the bandwidth of interest, we set its derivative to zero at the nominal point

$$\frac{dZ_{i2}(\omega_0)}{d\omega} = 0. \tag{4}$$

It suppresses the frequency sensitivity of $Z_{i2}(\omega)$ at ω_0, creating a relatively flat profile around the nominal point and ensuring $Z_{i2}(\omega) \approx R_2$. Conversely, we can set the derivative of $Z_{i1}(\omega)$ to a nonzero constant p as

$$\frac{dZ_{i1}(\omega_0)}{d\omega} = p \neq 0. \tag{5}$$

This constrains the slope of $Z_{i1}(\omega)$ at ω_0 and results in a quasilinear DPI profile. As a result, the $Z_{i1}(\omega)$ and DPI can be approximated as

$$Z_{i1}(\omega) = p\,(\omega - \omega_0) + R_1. \tag{6}$$

An example design is shown in Fig. 5, where the nominal point is set at 13.56 MHz with $R_1 = 100\,\Omega$ and $R_2 = 50\,\Omega$. We choose $p = 10\,\mu\Omega$s/rad to achieve a 50% DPI change within a 1 MHz bandwidth. Since the RRN has five unknown parameters

$$Z_{i1}^2(\omega) = (1-k^2)L_1^2 \frac{1-(1-k^2)L_2C_2\omega^2}{1-(1-k^2)L_1C_1\omega^2} \cdot \frac{1}{L_1C_1 + L_2C_2 - [(1-k^2)L_1L_2C_1C_2\omega^2 + \omega^{-2}]} \tag{1}$$

$$Z_{i2}^2(\omega) = (1-k^2)L_2^2 \frac{1-(1-k^2)L_1C_1\omega^2}{1-(1-k^2)L_2C_2\omega^2} \cdot \frac{1}{L_1C_1 + L_2C_2 - [(1-k^2)L_1L_2C_1C_2\omega^2 + \omega^{-2}]}. \tag{2}$$

while only four constraints are provided by (3) to (5), we have the flexibility to select $k = 0.9$ to simplify the calculation. A detailed discussion on the impacts of different values of p and k is given in the next section. Substituting the values into (3)–(5) yields the following circuit parameters:

$$L_1 = 11.58\,\mu\text{H}, \quad C_1 = 137.9\,\text{pF}$$
$$L_2 = 945.2\,\text{nH}, \quad C_2 = 917.7\,\text{pF}. \tag{7}$$

As illustrated in Fig. 5, the profile of $Z_{i2}(\omega)$ exhibits a flattened convex curvature around the nominal frequency. The figure depicts a 1 MHz bandwidth, with the maximum deviation of $Z_{i2}(\omega)$ from R_2 being approximately 10%, occurring at the frequency band's boundary. This corresponds to a reflection coefficient of 0.048, which validates the assumptions made in (4) and confirms that $Z_{i1}(\omega)$ governs the DPI profile. Fig. 5 compares $Z_{i1}(\omega)$, the amplitude of DPI, and their linear approximation from (6). All three curves closely align within the 1 MHz bandwidth, demonstrating the effectiveness of the proposed design methodology. The linearity of $Z_{i1}(\omega)$ is preserved relative to its tangent line, while the DPI closely tracks $Z_{i1}(\omega)$ due to the nearly constant characteristics of $Z_{i2}(\omega)$. Although the mismatch slightly increases at lower frequencies, the overall maximum-to-minimum impedance ratio of the DPI remains consistent with the predicted value from $Z_{i1}(\omega)$, approximately doubling from low to high frequencies within the band. Further calculations show that the phase of the DPI stays between 0° and -4° over the plotted frequency range, indicating that a near-resistive DPI is achieved. Thus, through engineering approximations, we can assume the RRN is ideal within the bandwidth of interest, disregarding the small nonideal phase deviation. As a result, the DPI can be considered approximately equal to the resistive Z_{i1}. In conclusion, the example RRN with the ICDT topology validates the proposed design approach, demonstrating the ability to achieve doubled power modulation across a 1 MHz tuning bandwidth.

C. Parameter Analysis

The performance of an RRN depends on its specific topology and circuit parameters. For instance, an ICDT network designed with different p values can exhibit varying power modulation sensitivity, while both p and k values influence the bandwidth and reactive current within the network. To examine these effects, we use the ICDT RRN as a case study, focusing on the following figures of merit (FOMs).

1) *Nominal bandwidth* (BW) is defined based on a maximum tolerable $Z_{i2,\text{max}}$. If $\omega_l \le \omega \le \omega_h$ represents the largest frequency band where $Z_{i2}(\omega) \le Z_{i2,\text{max}}$, then the bandwidth is given by $BW = \omega_h - \omega_l$. Its value is normalized to the nominal angular frequency ω_0. We assume $Z_{i2} \approx R_2$ is valid within the bandwidth, and Z_{i1} and DPI exhibit nearly identical profiles. Note that this definition only applies to the specific topology studied in this section. With a different RRN topology, the analysis approach might change, and the margin could be set differently. For instance, if the Z_{i2} curve becomes concave instead of convex, a minimum Z_{i2} ($Z_{i2,\text{min}}$) may need to be defined.
2) *Nominal power modulation ratio* (χ) is defined as the ratio of the maximum to minimum values of DPI within the band that defines BW.
3) *Peak reactive current* I_{pk} is the maximum peak current flowing in the RRN at the nominal frequency. Its value is normalized to the load current.

For the following discussion, we use normalized values to simplify the analysis and generalize the conclusions. In addition to the FOMs, the frequency is normalized to the nominal value ω_0, $Z_{i1}(\omega)$ is normalized to R_1, and $Z_{i2}(\omega)$ is normalized to R_2.

Fig. 6 shows the performance of the ICDT RRN with identical image impedance derivatives but varying coupling coefficient k. We maintain the same setting of $R_1 = 2R_2$ as in the previous example. As depicted in the figure, both $Z_{i1}(\omega)$ and $Z_{i2}(\omega)$ exhibit consistent overall trends as k changes. When k decreases, the curvature of $Z_{i2}(\omega)$ becomes more pronounced, leading to a reduced flat section around the nominal frequency. This indicates that the first-order approximation of image impedances remains valid over a narrower bandwidth. To quantify this effect, we set $Z_{i2,\text{max}}$ to be 10% higher than R_2 and analyze the impact of varying k on the FOMs, as shown in Fig. 6. Notice that the normalized profiles of BW and χ are nearly identical, differing only by a scaling factor. This indicates that even for small k, the DPI maintains good linearity within the narrowed bandwidth. It also suggests that the proposed RRN methodology is applicable across a wide range of coupling coefficients in the ICDT network. The general trends in Fig. 6 demonstrate that an increased k leads to both a wider nominal BW and a higher power modulation ratio (χ), while reducing the peak reactive current (I_{pk}). Since a lower reactive current typically enhances system efficiency, a larger coupling coefficient is generally desirable, provided the amplifier can operate across the required bandwidth.

To analyze how different image impedance derivatives affect the RRN's performance, we define the normalized slope of $Z_{i1}(\omega)$ as follows:

$$\hat{p} = \frac{\omega_0}{R_1} p. \tag{8}$$

With a fixed coupling coefficient of 0.95 and $R_1 = 2R_2$, the result of changing $\hat{p}$ is summarized in Fig. 7. The FOMs are calculated with the same $Z_{i2,\text{max}}$ of 110% of R_2. As $\hat{p}$ increases, $Z_{i1}(\omega)$ displays the expected quasilinear profile around the nominal frequency with a steeper slope. Meanwhile, $Z_{i2}(\omega)$ curls upward, leading to a narrower bandwidth. This reduced bandwidth counteracts the increased frequency sensitivity of the DPI, leading to diminishing returns when boosting χ. In addition, a higher $\hat{p}$ leads to a proportional increase in the peak reactive current, reducing the system's efficiency. Therefore, practical designs must balance power modulation capability with efficiency, and a moderate value of $\hat{p}$ is likely to offer the best overall performance.

By combining Figs. 6 and 7, we can conclude that the ICDT RRN can comfortably achieve approximately a twofold power modulation with reasonably chosen parameters. It is important to note that the discussion in this section applies specifically

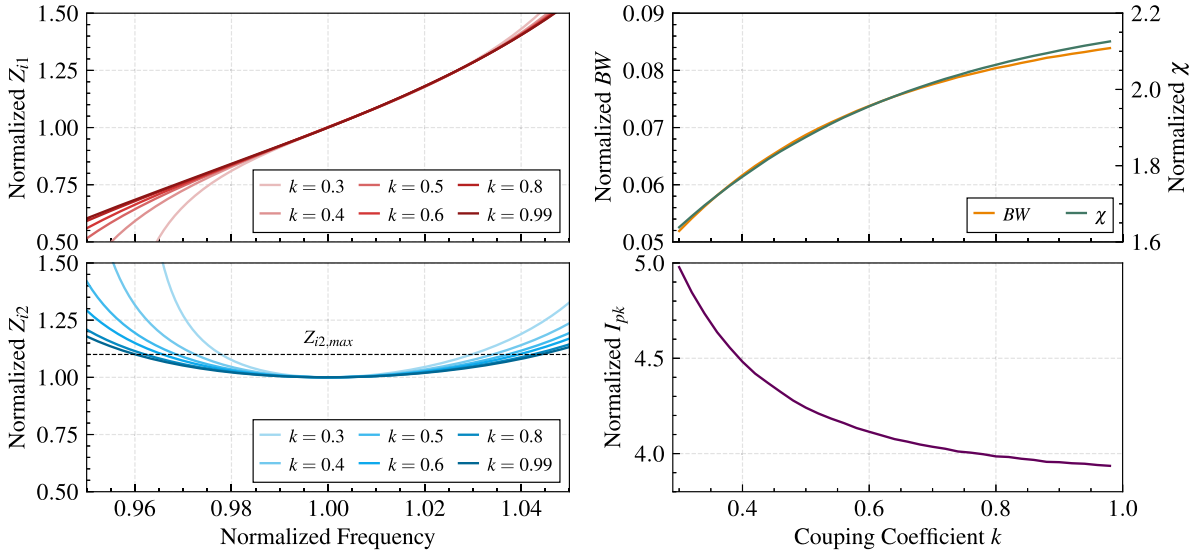

Fig. 6. ICDT RRN performance curves with varying coupling coefficients k and a fixed image impedance slope. The image impedance curves on the left show the profiles of $Z_{i1}(\omega)$ and $Z_{i2}(\omega)$ for different values of k. On the right, the FOM curves demonstrate the influence of k on the nominal bandwidth BW, the nominal power modulation ratio χ and the peak reactive current I_{pk} of the RRN. All values are normalized as per Section II-C.

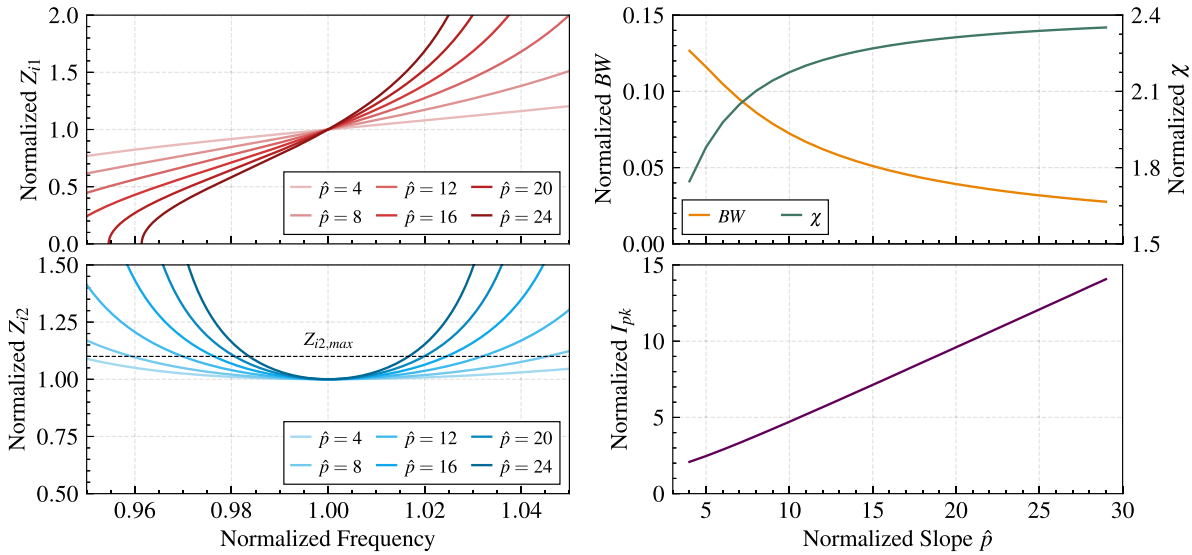

Fig. 7. ICDT RRN performance curves with varying load port's image impedance slope p and a fixed coupling coefficient. The image impedance curves on the left show the profiles of $Z_{i1}(\omega)$ and $Z_{i2}(\omega)$ for different values of the normalized slope $\hat{p}$. On the right, the FOM curves demonstrate the influence of $\hat{p}$ on the nominal bandwidth BW, the nominal power modulation ratio χ and the peak reactive current I_{pk} of the RRN. All values are normalized as per Section II-C.

to the ICDT network; RRNs with other topologies can behave differently. However, the general design methodology remains valid, and similar analyses can be conducted to assess the design parameters of those networks.

The impedance conversion ratio also plays a critical role in RRN design. While a different conversion ratio may not affect the normalized FOMs, it can still change the overall reactive power consumed by the network. Similar to conventional matching networks, a larger conversion ratio typically results in a higher quality factor, which can reduce the network's efficiency and tuning feasibility. Moreover, the impedance conversion ratio also impacts the PA design, which must be capable of driving the resulting DPI while delivering the desired power. Therefore, a moderate conversion ratio is generally more practical, as it balances the performance of both the PA and the RRN.

To qualitatively illustrate the impact of load variation on the RRN, Fig. 8 shows the DPI of the loaded RRN with nonideal load impedance. As shown in the figure, a deviation in resistance primarily scales the amplitude and phase of the DPI, while a deviation in reactance primarily causes a frequency shift in the DPI's amplitude and phase. Notably, with moderate load deviation ($\pm 10\%$), the RRN can still maintain a relatively resistive DPI and achieve noticeable power modulation. In addition, we expect

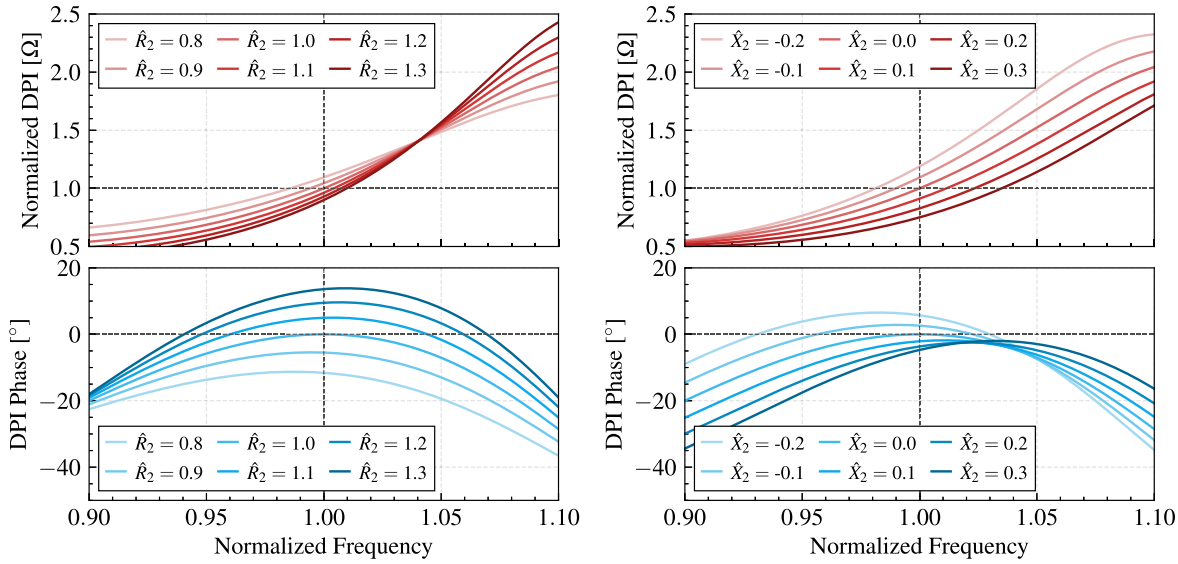

Fig. 8. ICDT RRN's DPI when loaded by nonideal impedance $\hat{R}_2 + j\hat{X}_2$ (normalized by R_2). The DPI curves on the left show the amplitude and phase for different values of normalized $\hat{R}_2$ with fixed $\hat{X}_2 = 0$. The curves on the right demonstrate the influence of nonzero normalized $\hat{X}_2$ on the DPI's amplitude and phase with nominal $\hat{R}_2 = 1$.

that the proposed RRN can be integrated with other techniques to mitigate load variations and enhance system performance in applications where varying loads are a addressed [25], [26], [27].

III. Switched-Mode Broadband PA

The implementation of the RRN requires a broadband PA with sufficient bandwidth, and switched-mode PAs are favored over linear ones due to their superior efficiency. Recent studies have shown promising advancements in broadband switched-mode PA designs with various topologies [28], [29], [30], and a general design methodology has been introduced in [31]. We apply this methodology, partitioning the amplifier into a switched network and a broadband filter, to carry out the design of a broadband class-Φ_2 PA in this section. We analyze the loading effect separately on the switched network and filter when driving the RRN across a broad bandwidth. A holistic amplifier design is given at the end of this section, combining all three circuit stages: the switched network, the broadband filter, and the RRN.

A. Class-Φ_2 Switched Network

The schematic of a typical class-Φ_2 PA is shown in Fig. 9, where the switched network contains L_F, C_F, L_{MR}, C_{MR}, and the semiconductor switch. We set the amplifier's nominal operating frequency to 13.56 MHz when driving the nominal load resistance $R_1 = 100\,\Omega$. According to [31], a high-Q condition is necessary for broadband operation and imposes a constraint on the maximum L_F, given by

$$L_F = \frac{R_1}{\omega_0 Q_F} \tag{9}$$

where ω_0 is the nominal angular frequency and Q_F is the desired quality factor. We choose $Q_F = 3.5$ for a moderate resonating current in the switched network, leading to an L_F of 335 nH. To

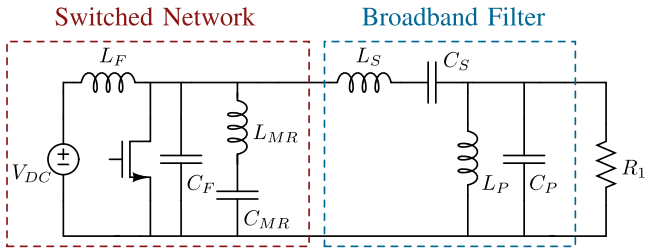

Fig. 9. Schematics of the broadband class-Φ_2 PA driving a load resistance of R_1.

account for the nonlinear C_{oss} of the semiconductor switch, we extend its ON-state time to 80% of the OFF-state time, resulting in a duty cycle of $D = 0.44$. The pole frequencies of the network, ω_a and ω_b, can thus be calculated by solving the following equations [31]:

$$\begin{aligned} \tan\left(\pi D' \frac{\omega_a}{\omega_0}\right) + \pi D \frac{\omega_a}{\omega_0} &= 0 \\ \tan\left(\pi D' \frac{\omega_b}{\omega_0}\right) + \pi D \frac{\omega_b}{\omega_0} &= 0 \end{aligned} \tag{10}$$

where $D' = 1 - D$. A shape factor of $r = 0.4$ is chosen to render a moderately flat voltage waveform across the switch (v_{ds}), and the shunt capacitance C_F can be determined as [31]

$$C_F = \frac{r + \left|\frac{\cos\left(\pi D' \frac{\omega_a}{\omega_0}\right)}{\cos\left(\pi D' \frac{\omega_b}{\omega_0}\right)}\right|}{L_F\left(r\omega_b^2 + \left|\frac{\cos\left(\pi D' \frac{\omega_a}{\omega_0}\right)}{\cos\left(\pi D' \frac{\omega_b}{\omega_0}\right)}\right|\omega_a^2\right)} = 165\,\text{pF}. \tag{11}$$

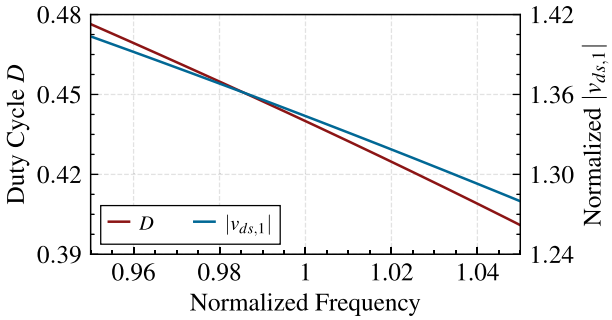

Fig. 10. Required duty cycle values for the designed class-Φ_2 switched network to achieve ZVS at different frequencies. The resulting fundamental component of the switch's drain-to-source voltage, $|v_{\mathrm{ds},1}|$, shows a negative frequency dependency.

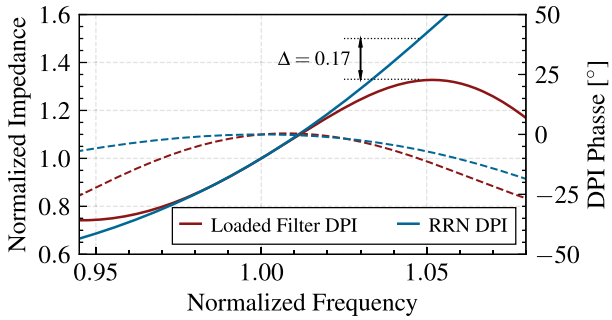

Fig. 11. Normalized DPI curves showing the RRN's loading effect on the filter. The filter is loaded by the same RRN, as shown in the figure. The amplitude of DPI is plotted with solid lines, while the phase is plotted with dashed lines.

Finally, the following equations render the required MR branch parameters [31]:

$$C_{\mathrm{MR}} = \frac{\omega_a^{-2}+\omega_b^{-2}}{L_F} - \frac{\omega_a^{-2}\omega_b^{-2}}{L_F^2 C_F} - C_F = 82\,\mathrm{pF}$$
$$L_{\mathrm{MR}} = \frac{\omega_a^{-2}\omega_b^{-2}}{L_F C_F C_{\mathrm{MR}}} = 363\,\mathrm{nH}. \tag{12}$$

When the RRN is driven by an amplifier, the RRN introduces loading effects that cause deviations from the intended nominal operation. These nonidealities can cause the amplifier to lose ZVS at high or low frequencies, ultimately restricting the range for frequency control and power modulation. With the aforementioned class-Φ_2 network design, it is beneficial to implement the RRN with a positive $Z_{i1}(\omega)$ slope for the following reasons.

1) Even though the output voltage of the class-Φ_2 network maintains consistent overall shape and amplitude, its fundamental component can have a slightly negative frequency dependency. Fig. 10 illustrates the required duty cycle at different frequencies to achieve ZVS and the resultant fundamental amplitude of the switch's drain-to-source voltage $|v_{\mathrm{ds},1}|$ [31]. A detailed derivation of the curves is included in Appendix A. It is evident that $|v_{\mathrm{ds},1}|$ drops by approximately 5% when the frequency is increased off the nominal value by the same percentage. Hence, it maximizes the power modulation ratio when combined with an RRN that has a positive impedance slope.
2) A positive $Z_{i1}(\omega)$ slope also helps maintain the high-Q condition needed for the amplifier to operate across a broad band. As shown in (9), for a given L_F, the desired quality factor Q_F is proportional to the ratio of the load resistance and the frequency. A large positive frequency slope of the DPI mitigates the degradation of Q_F as frequency decreases, extending ZVS operation to low frequencies. On the other hand, a negative frequency slope leads to a significantly reduced Q_F at high frequencies, abruptly restricting the bandwidth where ZVS is achievable.

Because the loading effect reduces the quality factor of the switched network on one side of the bandwidth, the PA with RRN will have asymmetric power modulation performance below and above the nominal frequency. For example, with a positive $Z_{i1}(\omega)$ slope, the PA is able to operate further above the nominal frequency than below without losing ZVS. Hence, the maximum power that the PA is able to output is set by the lowest frequency at which ZVS is maintained.

B. Broadband Filter

Theoretically, there is no constraint on the type of broadband filter that can be implemented with a broadband class-Φ_2 amplifier. We select the topology shown in Fig. 9 with the tuning proposed by Xu et al. [32] to demonstrate a practical design and discuss its performance when loaded by an RRN. As in [32], the two resonant branches resonate at the same nominal angular frequency ω_0, and their quality factors are defined as

$$Q_P = \frac{R_1}{\omega_0 L_P} = \omega_0 C_P R_1, \quad Q_S = \frac{\omega_0 L_S}{R_1} = \frac{1}{\omega_0 C_S R_1}. \tag{13}$$

Intuitively, the two resonant branches counteract each other near the nominal frequency, leading to a relatively flat passband [29]. For demonstration, we use the same nominal conditions as in [32], with $R_1 = 100\Omega$ at 13.56 MHz, and set $Q_S = 3$ and $Q_P = 2$. The resulting circuit parameters are

$$L_S = 3.6\,\mu\mathrm{H}, \quad C_S = 39\,\mathrm{pF}$$
$$L_P = 594\,\mathrm{nH}, \quad C_P = 230\,\mathrm{pF}. \tag{14}$$

Since the RRN exhibits a varying DPI across frequencies, the loading on the filter also changes accordingly. When the RRN's DPI deviates from its nominal value R_1, the filter's bandpass characteristics become less ideal, leading to increased signal attenuation and reflection. As a result, the filter's DPI seen by the switched network can no longer be assumed to match the RRN's DPI. This nonideal loading effect depends on the specific topology and implementation of the broadband filter. Careful filter design can mitigate this effect within the desired frequency range. Fig. 11 compares the DPI of the designed filter with the loading RRN's DPI. The comparison shows that around the nominal frequency, the two DPI curves overlap completely, indicating good passband characteristics. As the frequency deviates from the nominal value, the DPI of the loaded filter exhibits a diminishing derivative compared to the RRN's DPI, leading to a reduced power modulation ratio. The filter's attenuation becomes more pronounced at higher frequencies,

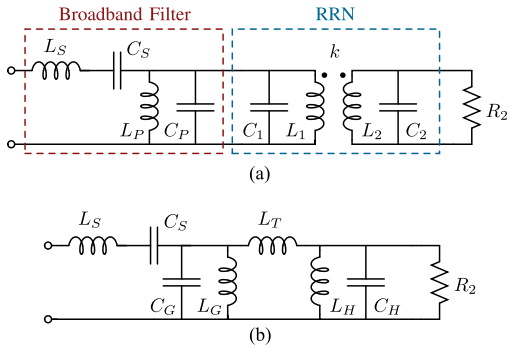

Fig. 12. Schematics showing the equivalent circuit combining the broadband filter and the RRN. (a) Conceptual circuit of the filter and the RRN for design. (b) Decoupled and simplified equivalent circuit.

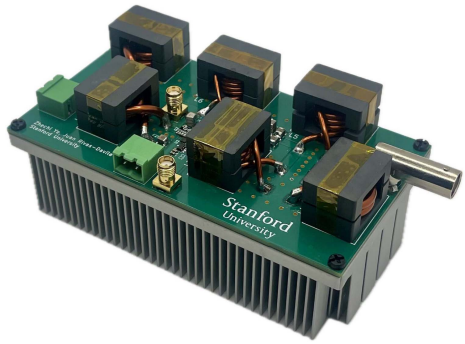

Fig. 13. Photograph of the PA prototype. The total dimensions are 5.2 in × 2.75 in × 2.15 in.

and we observe two key effects after the DPI's amplitude saturates: 1) The DPI amplitude begins to drop, reducing the loaded quality factor of the switched network and ultimately leading to a loss of ZVS. 2) The phase of DPI reduces and it becomes more capacitive. Qualitatively speaking, this capacitive load counteracts the discharging of the switch's shunt capacitance (C_F) before turn-ON, which negatively impacts ZVS. Since the lowest achievable output power corresponds to the highest impedance—and ZVS may still be maintained at this point—we conclude that the power modulation ratio in this case is primarily limited by filter attenuation, rather than ZVS loss.

In summary, the switched network and the broadband filter are impacted by the RRN's loading effects differently. For the special case studied in this section, if the RRN is designed with a positive $Z_{i1}(\omega)$ slope, the switched network helps increase the nominal power modulation ratio while the broadband filter attenuates it. The lowest tuning frequency is limited by the switched network to achieve ZVS, setting the maximum possible output power; the highest tuning frequency is limited by the filter attenuation, determining the lowest output power. As a result, the practical achievable power modulation is controlled by an asymmetric frequency tuning range around the nominal frequency. Further illustration of the loading effect is shown in Section IV, where a 13.2–14.4 MHz tuning range is achieved with a nominal frequency of 13.56 MHz.

C. Broadband PA With RRN Loading

As discussed in Section II-C, it is beneficial to design the RRN with a large coupling coefficient. Although achieving $k > 0.9$ with practical coupled inductors is challenging, the RRN's topology can be transformed into decoupled equivalent circuits, which are easier to implement. Moreover, the RRN can be integrated with the broadband filter stage in the PA, further simplifying the circuit and reducing the component count. Fig. 12 illustrates the conversion that combines the filter and the RRN. The converted component values are related to the original circuit as

$$C_H = C_2, \quad L_T = \frac{1-k^2}{k}\sqrt{L_1 L_2}$$

$$C_G = C_P + C_1, \quad L_H = \frac{1-k^2}{1-k\sqrt{L_1/L_2}}L_2$$

$$L_G = \left(\frac{1-k^2}{1-k\sqrt{L_2/L_1}}L_1\right) \| L_P. \tag{15}$$

In our experimental demonstration, we want to use the designed broadband PA to drive an RRN with $k = 0.99$ and $\hat{p} = 16$ for $R_1 = 2R_2 = 100\,\Omega$. Following the methodology proposed in Section II, the RRN parameters can be calculated as

$$L_1 = 128.6\,\mu\text{H}, \quad C_1 = 130\,\text{pF}$$
$$L_2 = 9.35\,\mu\text{H}, \quad C_2 = 892\,\text{pF}. \tag{16}$$

Combining with the filter stage parameters designed in (14) renders the component values for the equivalent circuit in Fig. 12(b) as

$$L_H = 254\,\text{nH}, \quad C_H = 892\,\text{pF}, \quad L_T = 697\,\text{nH}$$
$$L_G = 1564\,\text{nH}, \quad C_G = 359\,\text{pF}. \tag{17}$$

Notice that the inductor values are significantly reduced by a hundred times. This conversion alleviates the challenges of implementing large inductors with high coupling while keeping the same power modulation capability. With the combined PA and the RRN, its output power profile can be approximated by assuming an ideal broadband amplifier design [31]

$$P_{\text{out}} \approx \frac{|V_{ds,1}|^2}{2|Z_{\text{DPI,filter}}(\omega)|}. \tag{18}$$

This analytical profile is compared with simulation and experimental results in Fig. 15, indicating a good agreement between the analysis and experiment.

IV. Experiment and Discussion

A. Experimental Verification

We construct a 300 W PA prototype with RRN based on the design in Section III. The prototype is implemented with a GaN transistor on a 100–150 V dc bus. A detailed description of components in the prototype is listed in Table II, and a picture of the constructed amplifier is shown in Fig. 13.

To verify the power modulation capability of the proposed design, we tested the prototype across a frequency range of

TABLE II
CLASS-Φ_2 AMPLIFIER WITH RRN IMPLEMENTATION

Component	Description
L_F	335 nH, Fair-rite 67 EEQ25/16, AWG 8
L_{MR}	363 nH, Fair-rite 67 EEQ25/16, AWG 8
L_S	3.6 μH, Fair-rite 67 EEQ25/16, AWG 14
L_G	1.56 μH, Fair-rite 67 EEQ25/16, AWG 12
L_T	697 nH, Fair-rite 67 EEQ25/16, AWG 12
L_H	254 nH, Fair-rite 67 EEQ25/16, AWG 8
C_F	165 pF, including device C_{oss}, C0G ceramic
C_{MR}	82 pF, C0G ceramic
C_S	39 pF, C0G ceramic
C_G	259 pF, C0G ceramic
C_H	892 nF, C0G ceramic
Switch	GaNSystems GS66504B, 650 V eGaN FET
Gate Driver	Texas Instruments LMG1025

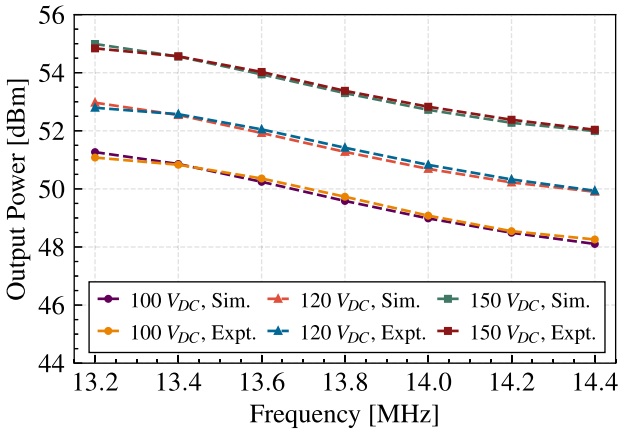

Fig. 14. Experimental and simulated output power of the prototype at different frequencies and DC voltages.

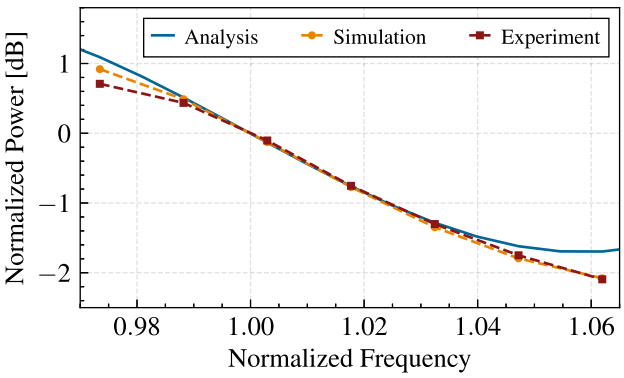

Fig. 15. Normalized power–frequency profiles comparing the theoretical analysis, simulation, and experiment. The curves are normalized to the frequency and power at the nominal condition.

13.2–14.4 MHz. Figs. 14 and 16 illustrate the experimental output power and drain efficiency of the prototype at various frequencies and dc voltages. An N1914 A RF power meter is used to measure the output power, while the input power is

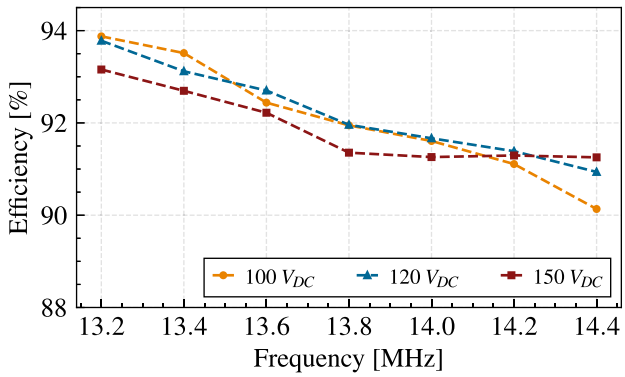

Fig. 16. Experimental efficiency measured at different frequencies and DC voltages.

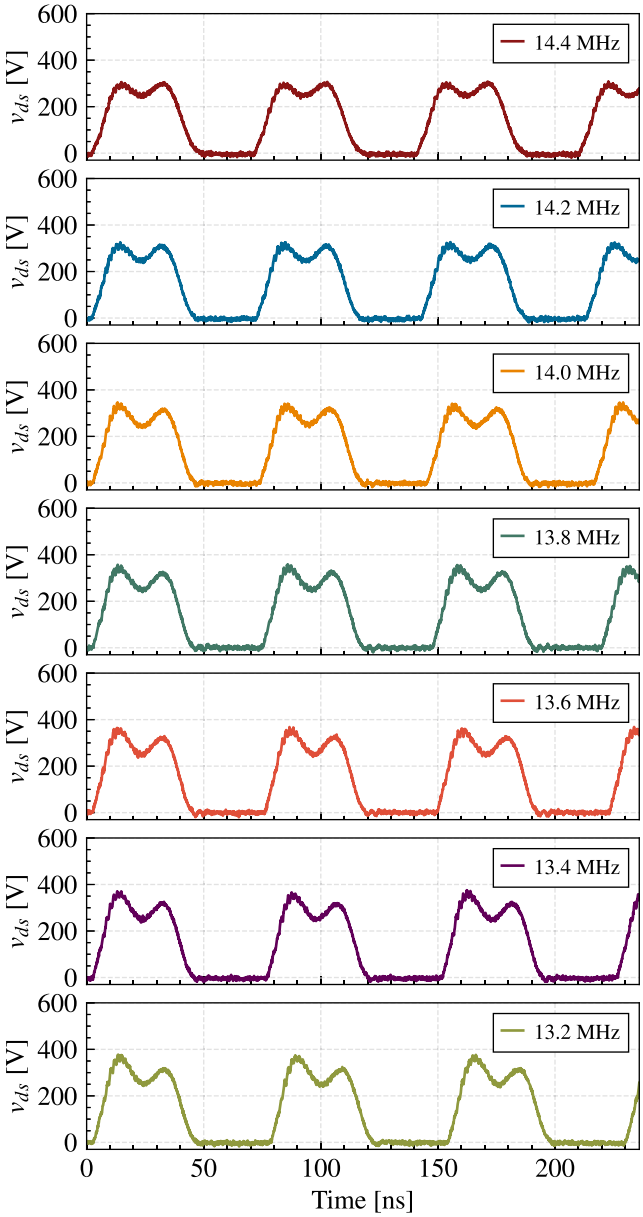

Fig. 17. Experimentally measured drain-to-source voltage v_{gs} waveform across the semiconductor device at 150 V DC input and different frequencies.

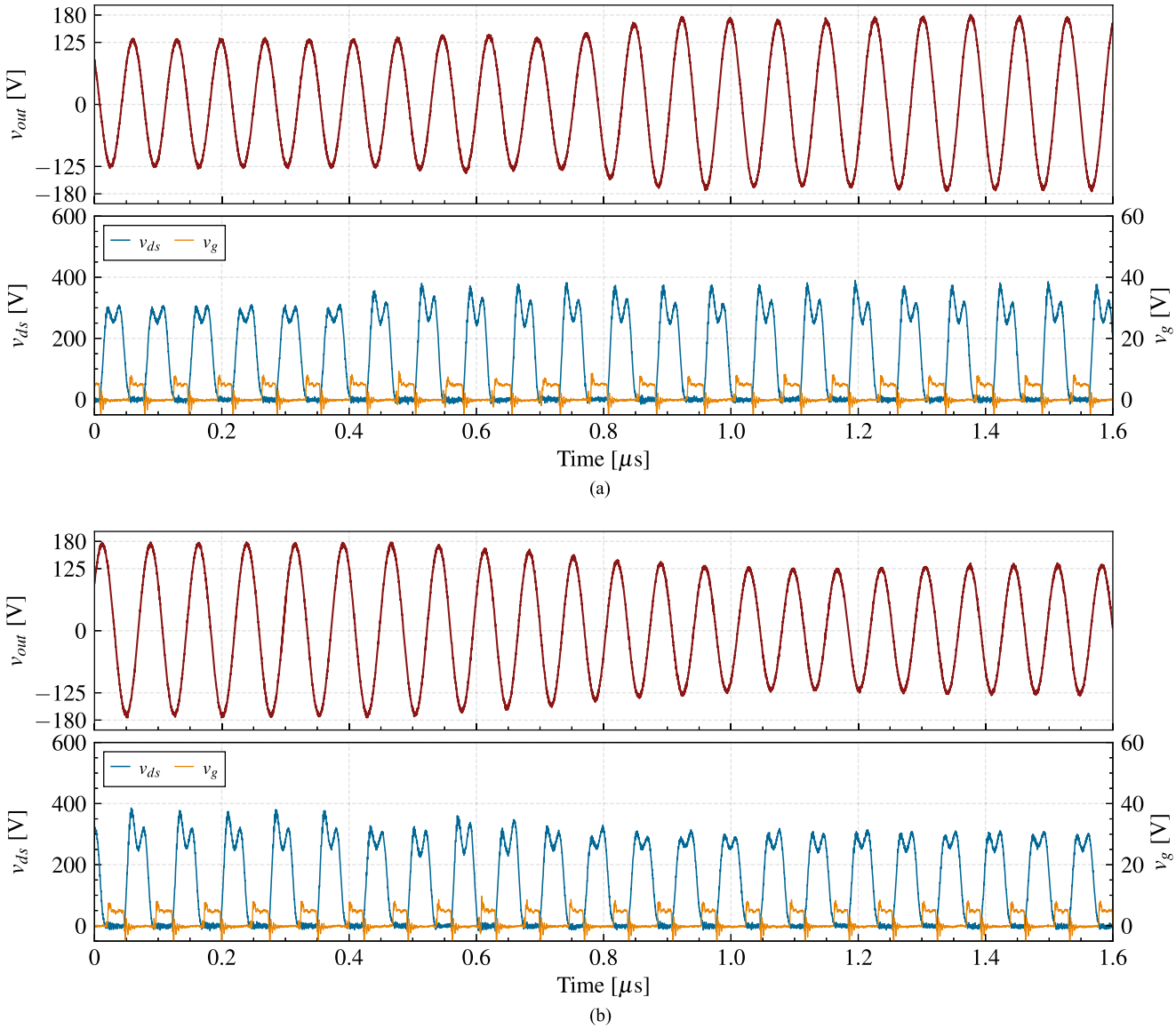

Fig. 18. Experimental waveform showing the transitions of power modulation. The DC input voltage is kept constant at 150 V. The drain-to-source voltage v_{ds} across the semiconductor device is plotted with its gate voltage v_g to illustrate the timing adjustment. (a) Frequency step from 14.4 to 13.2 MHz, output power transition from 160 to 300 W. (b) Frequency step from 13.2 to 14.4 MHz, output power transition from 300 to 160 W.

monitored using an N5771 A dc power supply. The results show good agreement between the simulation and experimental data. With a 150 V dc input, the amplifier prototype can generate 304.7 W (54.84 dBm) at 13.2 MHz and 159.8 W (52.03 dBm) at 14.4 MHz. The overall power modulation ratio achievable through frequency control is 1.91 (2.81 dB). As illustrated in Fig. 14, we anticipate that the power modulation range could be further enhanced by at least twofold with the addition of supply rail modulation, suggesting significant improvements in the dynamic range.

Fig. 15 further compares the normalized power–frequency profiles from analysis, simulation, and experiment. The three curves exhibit the same trend and overlap near the nominal frequency. As discussed in Section III, when the frequency drops below 13.2 MHz, the broadband amplifier loses ZVS due to a decrease in the quality factor of the switched network. On the other hand, frequencies above 14.4 MHz lead to additional attenuation by the filter network, resulting in significant impedance mismatch, output power saturation and eventually non-ZVS switching. As a result, the deviation between experiment and analysis increases, and the proposed design methodology is valid only within this frequency range.

The drain voltage waveform is captured using an N2875 A probe with an MSO9404 A oscilloscope, as shown in Fig. 17. The waveform shape is consistent across the entire bandwidth, and the smooth decline indicates that ZVS is maintained. As the frequency decreases from 14.4 to 13.2 MHz, the duty cycle increases, as predicted by Fig. 10. Due to the lower quality factor of the switched network at 13.2 MHz, the waveform shape becomes slightly distorted, resulting in an increase in

the peak voltage across the semiconductor switch. However, this distortion is minimal, and the overall performance of the amplifier remains unaffected.

The transitions of power modulation are captured and shown in Fig. 18. Fig. 18(a) depicts the transition from 160 to 300 W as the frequency and duty cycle are adjusted from 14.4 to 13.2 MHz. As shown in the figure, the transition is smooth without significant overshoots. The steady state is reached within a few switching cycles, approximately 500 ns. Fig. 18(b) shows a similar dynamic response in the opposite direction, with a slightly longer transition time of approximately 800 ns. It is also worth noting that ZVS is maintained during the entire transitions, ensuring efficient operation of the PA.

B. Discussion on Opportunities and Challenges

Theoretically, the proposed image-impedance-based approach is quite general and applicable to any two-port network, including those using distributed circuits, such as transmission lines. Therefore, the methodology should be scalable to higher frequency bands, such as ultrahigh frequency and beyond. In practice, however, challenges arise as parasitic elements become more pronounced at higher frequencies, potentially impacting the performance of the RRN. To mitigate these effects, careful selection of components with low parasitics, along with the use of advanced PCB design techniques (e.g., minimizing trace lengths, ensuring proper grounding, and implementing shielding), would be necessary to maintain performance and effectively implement RRNs at these higher frequency ranges.

The demonstrated high efficiency and fast power modulation capabilities of the proposed RRN present a significant opportunity for a wide range of applications, including wireless communication systems, radar and remote sensing technologies, medical imaging devices, and wireless power transfer (WPT) systems. In particular, the ability of the RRN to dynamically adjust power output with rapid response times and minimal energy loss is highly advantageous in applications that require real-time power regulation and adaptability. For instance, in MRI, the fast power modulation offered by the RRN could contribute to more efficient RF and gradient (shimming) amplifier designs [4], [33], potentially reducing the cost and improving the accessibility of MRI scanners. Furthermore, in WPT systems, the passive nature of the RRN makes it highly compatible with both inductive power transfer (IPT) and capacitive power transfer (CPT) setups. The RRN can be integrated with transmitter and receiver coils in IPT systems or with plates in CPT systems, enabling fast, precise, and efficient modulation of power. Overall, the versatility and high performance of the RRN in managing power delivery make it a strong candidate for next-generation power modulation solutions across diverse fields. Its ability to maintain efficiency while delivering fast, precise power control sets it apart as a key technology for future RF and power transfer systems.

V. Conclusion

In this article, we propose a novel approach for fast RF power modulation using an RRN through frequency adjustment. We outline the general methodology and provide detailed design guidelines, using the ICDT topology as an illustrative example. In addition, we examine the impact of the RRN's loading effects on the broadband PA. To validate the proposed method, we implement a 300 W broadband class-Φ_2 PA integrated with an RRN. The results demonstrate ultrafast power modulation from 13.2 to 14.4 MHz, with high efficiency maintained throughout.

The proposed frequency-controlled power modulation with the RRN complements existing methods, such as voltage rail regulation and out-phasing. It can be integrated with various modulation techniques to enhance transient response and achieve a higher dynamic range. A holistic design and optimization that combines different power modulation approaches presents a valuable area for future research. Moreover, the RRN design methodology is applicable to arbitrary two-port topologies, offering further opportunities to explore new circuit implementations.

Appendix A
Switched-Network Equations

According to [31], normalized OFF-state transient response v_F of a class-Φ_2 switched network can be expressed as

$$\frac{v_F(D,\omega,t)}{V_{DC}} = A\left(\pi D\frac{\omega_a}{\omega}\sin(\omega_a t)-\cos(\omega_a t)\right) + B\left(\pi D\frac{\omega_b}{\omega}\sin(\omega_b t)-\cos(\omega_b t)\right)+1 \quad (19)$$

where ω is the angular switching frequency, and

$$A=\frac{\omega_b^2-\frac{1}{L_F C_F}}{\omega_b^2-\omega_a^2},\quad B=\frac{\omega_a^2-\frac{1}{L_F C_F}}{\omega_a^2-\omega_b^2} \quad (20)$$

are parameters by design. At any angular switching frequency ω_s, the desired duty cycle can be calculated by solving

$$v_F(D)|_{\omega=\omega_s,\, t=D'T}=0. \quad (21)$$

And the fundamental component of the drain voltage is

$$v_{\mathrm{ds},1}(\omega)=2\,\mathcal{F}\left[v_F\left(D,\omega,t\right)\Pi_{D'T}\left(t-\frac{D'T}{2}\right)\right]\Big|_{\xi=\frac{1}{T}} \quad (22)$$

where $\mathcal{F}$ represents the Fourier transform with variable ξ, and $\Pi_{D'T}(t)$ is the rectangular function with a width of $D'T$. As a result, Fig. 10 can be plotted by solving (21) and (22) across the bandwidth of interest.

Acknowledgment

The authors would like to thank Dr. Lei Gu for the constructive discussions.

References

[1] D. Graves, "Plasma processing," *IEEE Plasma Sci.*, vol. 22, no. 1, pp. 31–42, Feb. 1994.
[2] C. H. Lin, Z. Ye, E. Stolt, and J. Rivas-Davila, "1 kW 6.78 MHz push-pull ϕ_2 amplifier for induction heating," in *Proc. 2024 IEEE Appl. Power Electron. Conf. Expo.*, 2024, pp. 595–599.
[3] F. H. Raab, "GaN-FET class-e amplifier for 60-MHz radar," in *Proc. 50th Eur. Microw. Conf.*, 2021, pp. 1099–1102.
[4] W. D. Braun, L. Gu, G. Scott, and J. Rivas-Davila, "MRI compatible dc modulator for an envelope tracking transmitter," in *Proc. 20th Workshop Control Model. Power Electron.*, 2019, pp. 1–4.

[5] C. Jung, K. Chi, B. Hwang, J. Moon, M. Lee, and J. Lee, "Advanced plasma technology in microelectronics," *Thin Solid Films*, vol. 341, no. 1, pp. 112–119, Mar. 1999.
[6] S. Samukawa and T. Mieno, "Pulse-time modulated plasma discharge for highly selective, highly anisotropic and charge-free etching," *Plasma Sources Sci. Technol.*, vol. 5, no. 2, May 1996, Art. no. 132.
[7] R. W. Boswell and R. K. Porteous, "Etching in a pulsed plasma," *J. Appl. Phys.*, vol. 62, no. 8, pp. 3123–3129, 1987.
[8] A. Agarwal et al., "Effect of simultaneous source and bias pulsing in inductively coupled plasma etching," *J. Appl. Phys.*, vol. 106, no. 10, 2009, Art. no. 103305.
[9] D. J. Economou, "Pulsed plasma etching for semiconductor manufacturing," *J. Phys. D: Appl. Phys.*, vol. 47, no. 30, 2014, Art. no. 303001.
[10] V. M. Donnelly and D. J. Economou, "Atomic layer etching with pulsed plasmas," U.S. Patent App. 12/966,844, Jun. 16 2011.
[11] M. B. Cohen, "ELF/VLF phased array generation via frequency-matched steering of a continuous HF ionospheric heating beam," Ph.D. dissertation, Stanford University, Stanford, CA, USA, 2009.
[12] J. Shoeb, A. Paterson, and Y. Wu, "Multi-level parameter and frequency pulsing with a low angular spread," U.S. Patent 10,224,183, Mar. 5, 2019.
[13] J. Shoeb, A. Paterson, and Y. Wu, "Multi-level pulsing of dc and RF signals," U.S. Patent 10,304,660, May 28, 2019.
[14] D. Shimizu, W. Lee, K. Kawasaki, L. Ling, P. Justin, and K. Choi, "Smart multi-level RF pulsing methods," U.S. Patent 9,872,373, Jan. 16, 2018.
[15] J. Staudinger et al., "High efficiency CDMA RF power amplifier using dynamic envelope tracking technique," in *Proc. 2000 IEEE MTT-S Int. Microw. Symp. Dig.*, 2000, vol. 2, pp. 873–876.
[16] V. Yousefzadeh, N. Wang, D. Maksimovic, and Z. Popovic, "Digitally controlled DC-DC converter for RF power amplifier," in *Proc. 19th Annu. IEEE Appl. Power Electron. Conf. Expo.*, 2004, vol. 1, pp. 81–87.
[17] H. Zhang et al., "High-efficiency wide-range RF power generation systems with discrete power back-off from multiple inverters," *IEEE Trans. Power Electron.*, vol. 40, no. 1, pp. 290–302, Jan. 2025.
[18] H. Chireix, "High power outphasing modulation," *Proc. Inst. Radio Eng.*, vol. 23, no. 11, pp. 1370–1392, 1935.
[19] T. Barton, "Not just a phase: Outphasing power amplifiers," *IEEE Microw. Mag.*, vol. 17, no. 2, pp. 18–31, Feb. 2016.
[20] D. J. Perreault, "A new power combining and outphasing modulation system for high-efficiency power amplification," *IEEE Trans. Circuits Syst. I: Reg. Papers*, vol. 58, no. 8, pp. 1713–1726, Aug. 2011.
[21] A. S. Jurkov, L. Roslaniec, and D. J. Perreault, "Lossless multiway power combining and outphasing for high-frequency resonant inverters," *IEEE Trans. Power Electron.*, vol. 29, no. 4, pp. 1894–1908, Apr. 2014.
[22] K. Surakitbovorn and J. M. Rivas-Davila, "Modular ON/OFF and phase-shifting for high-speed radio frequency power modulation," *IEEE Open J. Power Electron.*, vol. 1, pp. 393–406, 2020.
[23] O. J. Zobel, "Transmission characteristics of electric wave-filters," *Bell System Tech. J.*, vol. 3, no. 4, pp. 567–620, 1924.
[24] D. M. Pozar, *Microwave Engineering*, 4th ed. Chichester, U.K.: John Wiley & Sons, Inc., Nov. 2011.
[25] Z. Ye, K. Surakitbovorn, C. Lin, and J. Rivas-Davila, "Frequency-tuning matching network for load-varying applications," in *Proc. 2024 IEEE Appl. Power Electron. Conf. Expo.*, 2024, pp. 1604–1607.
[26] A. S. Jurkov, A. Radomski, and D. J. Perreault, "Tunable matching networks based on phase-switched impedance modulation1," *IEEE Trans. Power Electron.*, vol. 35, no. 10, pp. 10150–10167, Oct. 2020.
[27] J. Choi, J. Xu, R. Makhoul, and J. M. R. Davila, "Implementing an impedance compression network to compensate for misalignments in a wireless power transfer system," *IEEE Trans. Power Electron.*, vol. 34, no. 5, pp. 4173–4184, May 2019.
[28] Z. Tong, L. Gu, and J. Rivas-Davila, "Wideband PPT class ϕ_2 inverter using phase-switched impedance modulation and reactance compensation," *IEEE Trans. Ind. Electron.*, vol. 69, no. 6, pp. 5724–5734, Jun. 2022.
[29] Z. Tong and J. M. Rivas-Davila, "Wideband push-pull class E amplifier for RF power delivery," in *Proc. IEEE 24th Workshop Control Model. Power Electron.*, 2023, pp. 1–7.
[30] S. Chen and L. Gu, "A wideband push-pull ϕ_2 amplifier with PCB inductors and Rogowski coils for RF plasma generators," in *Proc. 2024 IEEE Workshop Control Model. Power Electron.*, 2024, pp. 1–6.
[31] Z. Ye and J. Rivas, "Broadband high frequency power conversion with frequency-tuning matching network," *IEEE Open J. Power Electron.*, vol. 6, pp. 120–129, 2025.
[32] J. Xu, Z. Tong, and J. Rivas-Davila, "1 kW MHz wideband class E power amplifier," *IEEE Open J. Power Electron.*, vol. 3, pp. 84–92, 2022.
[33] J. P. Stockmann et al., "A 32-channel combined RF and B shim array for 3T brain imaging," *Magn. Reson. Med.*, vol. 75, no. 1, pp. 441–451, 2016. [Online]. Available: https://onlinelibrary.wiley.com/doi/abs/10.1002/mrm.25587